International Journal of Hydrogen Energy 195 (2025) 152517

Contents lists available at ScienceDirect

International Journal of Hydrogen Energy

journal homepage: www.elsevier.com/locate/he

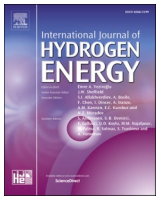

First-principles study of hydrogen desorption of Mg–Zr semi-co-sputtering films

Yongqing Wang [a], Junqing Ding [a], Zhijie Fang [a], Xingyu Zhou [a,*], Yu-Jun Zhao [b,c,**]

[a] Guangxi Key Laboratory of Multidimensional Information Fusion for Intelligent Vehicles, GuangXi University of Science and Technology, Liuzhou, 545006, China
[b] Department of Physics, South China University of Technology, Guangzhou, 510641, China
[c] Key Laboratory of Advanced Energy Storage Materials of Guangdong Province, South China University of Technology, Guangzhou, 510641, China

ARTICLE INFO

Keywords:
Co-lattice interlayer
Hydrogen desorption
Mg–Zr film

ABSTRACT

Previous experimental findings revealed that $Mg_{0.83}$-$Zr_{0.17}H_2$(111) films with modulated $3MgH_2+2ZrH_2$ layers exhibit significantly improved dehydrogenation performance. To understand the underlying mechanism, we conducted density functional theory (DFT) calculations to investigate the hydrogen desorption behavior of $Mg_{0.83}$-$Zr_{0.17}H_2$(111) thin films. Our results show that the incorporation of Zr increases the average interlayer spacing of the Zr-containing slab by approximately 0.10 Å compared to the pure-MgH_2(111) surface. This expansion is attributed to the elongation of Mg–H and Zr–H bonds at the coherent Mg–Zr interface, consistent with experimental observations. Electronic structure analysis reveals a positive charge accumulation at the Mg–Zr coherent interface, indicating interfacial electron redistribution. Furthermore, the partial density of states (PDOS) shows that H *s* orbital become more localized and sharper with Zr addition, suggesting altered bonding characteristics. The integrated crystal orbital Hamilton population (ICOHP) analysis demonstrates that the Mg–H bonds at the Mg–Zr interface are weakened, with bond strengths reduced by up to ~30 %, facilitating hydrogen desorption. These findings provide atomic-level insights into the enhanced dehydrogenation properties of Mg–Zr films and highlight the critical role of modulated interfacial structures in tuning hydrogen storage performance.

1. Introduction

The approaches of hydrogen storage in the vehicles powered by hydrogen energy have a critical impact on the applications [1–7]. Hydrogen storage by metal hydrides has been the focus of recent intensive researches [8,9]. Among them, MgH_2, whose theoretical storage reaches 7.6 wt% of hydrogen, exhibiting a high capacity of reversible hydrogen absorption and desorption. In addition, magnesium is also attractive for thermal energy storage due to its high enthalpy of hydride formation ($\Delta H = -75$ kJ/mol). Combined with other features, for example, low cost, abundant in the earth, magnesium has been widely studied in the hydrogen storage [10,11]. However, to date magnesium hydride remains of limited use for hydrogen storage. The main reason is that the reaction for hydrogenation and dehydrogenation is very slow, and the hydrogen desorption needs a high temperature about 300 °C. Many efforts, such as improving surface and kinetic properties by ball milling [12], alloying with other transition metal and their oxides [13–15], using catalyst [16,17], forming thin film hydride [18,19], have focused on reducing the desorption temperature and accelerating the reaction.

Thin-film nanostructuring introduces a high density of surfaces and hetero-interfaces that raise the total free energy of Mg-based hydrogen storage systems, thereby substantially enhancing their intrinsic reactivity. Consequently, film-downscaling is widely recognized to improve the storage performance of Mg through the following synergistic advantages: (1) the large surface/interface-to-volume ratio provides abundant low-coordination sites that facilitate H_2 dissociation on the film surface; (2) the shortened diffusion path for atomic hydrogen, together with the profuse grain boundaries present in multilayer composite films, offers preferred nucleation sites for the hydride phase and thus accelerates hydrogenation kinetics; and (3) the excess surface and interfacial energy supplies an additional thermodynamic driving force for hydride formation.

These combined effects have been experimentally verified to deliver

* Corresponding author. Guangxi Key Laboratory of Multidimensional Information Fusion for Intelligent Vehicles, GuangXi University of Science and Technology, Liuzhou, 545006, China.
** Corresponding author. Department of Physics, South China University of Technology, Guangzhou, 510641, China.
E-mail addresses: zhouxingyu2u@163.com (X. Zhou), zhaoyj@scut.edu.cn (Y.-J. Zhao).

https://doi.org/10.1016/j.ijhydene.2025.152517
Received 16 June 2025; Received in revised form 26 October 2025; Accepted 8 November 2025
Available online 12 November 2025

significant improvements in both absorption/desorption rates and operating temperature windows for Mg thin-film systems. Ayshe et al. [20] prepared pure Mg films (50–1000 nm) with Pd capping by thermal evaporation, they found that the films with thickness over 200 nm were difficult to be fully hydrogenated, and the dehydrogenation temperature of the films became higher as the thickness increased. Higuchi et al. [21] prepared Mg (200 nm) films capped with Pd (25 nm) by magnetron sputtering, and the films could reach a hydrogen storage capacity of 6.6 wt% after hydrogenation at 1 bar at 100 °C for 24 h. The dehydrogenation peak occurred at 40–260 °C. Qu et al. [22] showed that the films with Mg layer thickness of 40 nm exhibit the fastest hydrogen absorption and desorption rates compared with 60, 80, 100 nm, which may be caused by the shorter diffusion paths of H atoms in the thinner films. Besides, it's found that the addition of catalyst into the Mg films would improve the hydrogen storage properties of films [23–25]. Such as the Mg (100 nm)-Ti (0.5, 1, 2, 4 nm)-Pd (10 nm) films can absorb and desorb hydrogen at room temperature [23], the hydrogen absorption and release temperature of Mg–Cu (5, 10, 15 at.%) thin films decreased gradually with the increase of Cu content [24].

Among of them, Zirconium is an effective additive to catalyze the hydrogen absorption and desorption reaction of magnesium [14,15,26,27]. Moreover, Zr possesses the same hexagonal close-packed (HCP) structure and a lattice constant nearly identical to that of Mg. Upon hydrogenation, the resulting MgH_2 and ZrH_2 both adopt the cubic $Fm\bar{3}m$ space group, ensuring a coherent interface is maintained. Therefore, it has been found that there is a Mg–Zr common-lattice heterogeneous interface in the Mg–Zr hydrogen storage system, which will facilitate the H diffusion and provide a large number of Mg/MgH_2 nucleation sites [28]. However, under normal preparation conditions, Mg and Zr are not miscible and do not form any alloy phase [29]. The corresponding Mg–Zr composites can be obtained only by some special preparation means, such as high-pressure synthesis method, thin-filming, etc. Checchetto et al. [15] produced Mg and Zr-doped Mg samples in form of thick films (thickness of 10–20 nm) on graphite wafers. Its dehydrogenation peak temperature was 262 °C, which was much lower than that of 357 °C for pure Mg films. They suggested that the improved dehydrogenation properties of the film are due to the presence of interfaces between Mg/MgH_2 and Zr, which act as heterogeneous nucleation sites for Mg, lowering its activation energy and providing a channel for rapid diffusion of H. Bao et al. [30] investigated the properties of $Mg_{(1-x)}Zr_x$ (x = 0.29, 0.24, 0.17) thin films. The hydrogen storage capacity of the films decreased gradually with increasing Zr content and the rate of hydrogen absorption and desorption increased; after hydrogenation, the Mg–Zr films were transformed into the Mg–Zr–H phase of face centered cubic (FCC).

In addition to the efforts on improving hydrogen storage effect by fabricating Mg films mentioned above, we prepared Mg_{1-x}-Zr_x (x = 0.13, 0.17, 0.25) semi-co-sputtering films [31] with a Pd covers, and three special Mg–Zr modulated structures occurred. The modulated structure is composed of 3–4 Mg(0002) atomic layers plus 1 to 3 Zr(0002) atomic layers in a period, with the Mg and Zr layers stacked in a staggered manner. After hydrogenation, the preferred orientation of the film changes from Mg–Zr(0002) to Mg–Zr–H(111) while $Mg_{0.83}$-$Zr_{0.17}$(0002) maintaining the modulated structure (3 Mg(0002) plus 2 Zr(0002) layers trun into 3 MgH_2(111) plus 2 ZrH_2(111) layers) as a whole. The presence of a large number of Mg–Zr(-H) heterogeneous lattice interfaces in Mg–Zr semi-co-sputtering films provides many Mg/MgH_2 nucleation sites and diffusion channels for H atoms. They concluded that the presence of Zr in the Mg–Zr semi-co-sputtering films improves the hydrogen absorption and desorption properties. Our previous calculations based on density functional theory (DFT) showed that the interfacial regions exhibit both a reduced interlayer spacing and tensile strain, accompanied by a redistribution of 3*d* electrons contributed by Zr, thereby corroborating the experimental observations.

To elucidate atomic-scale desorption behaviour, we herein model the hydrogen desorption process of pure-MgH_2(111) and $Mg_{0.83}$-$Zr_{0.17}H_2$(111) films. Owing to its ability to accurately describe electron interactions between atoms in periodic lattices, DFT was again selected for the present study. The results of bond strength calculations of $Mg_{0.83}$-$Zr_{0.17}H_2$(111) system also indicate that the Mg–H bond at the Mg–Zr co-lattice interface is the weakest and easily broken.

2. Computational details

According to the experiments, the $Mg_{0.83}$-$Zr_{0.17}H_2$(111) film has a modulation structure with 5 layers of Mg–Zr–H(111), 3 layers of MgH_2(111) plus 2 layers of ZrH_2(111), as a period. As the interface between MgH_2 and ZrH_2 is coherent, the similar crystal structure are found in the *Materials Project* [32]. The relevant structural parameters are listed in Table 1. Both MgH_2 and ZrH_2 have phases with a same space group ($Fm\bar{3}m$, No. 225), with the 2θ values of crystal plane (111) of the XRD pattern are around 32.567° and 32.176°, respectively. It is established that the alloys of MgH_2 and ZrH_2 could be indeed co-lattice respectively in the Mg–Zr films.

Regarding the construction of the modulation structure, we reconstructed the lattice and then replaced certain layers of Mg atoms with Zr atoms. The detailed approach is shown in Fig. 1. We set new lattice vectors, (1 0–1), (0 1 -1) and (1 1 1), in terms of the old lattice of (1 0 0), (0 1 0) and (0 0 1), along *a*, *b* and *c* respectively of MgH_2 unit cell to redefine lattice. Then, volume of the new cell is 3 times that of the MgH_2 conventional cell. As the new cell has three layers of Mg atoms, and the modulation structure obtained experimentally takes 5 layers as the minimum period, so we take the least common multiple of the two numbers, that is, the cell of 15 layers of MgH_2 plus ZrH_2 is built as the simulation structure of $Mg_{0.83}$-$Zr_{0.17}H_2$ modulation structure in this work. Finally, the unit cell of $Mg_{0.83}$-$Zr_{0.17}H_2$ was optimized and cleaved to obtain the $Mg_{0.83}$-$Zr_{0.17}H_2$(111) surface. Since it was found experimentally [31] that the diffraction peak of Pd had disappeared after repeated hydrogen absorption and desorption, the model of Pd capping was not considered in this work.

Table 2 gives the structure parameters and formation energies of Mg_{1-x}-Zr_xH_2 (x = 0, 0.17). The atomic coordinates were fully relaxed to obtain optimized model structures. The formation energy is defined by

$$E_{\text{form}} = \left(E_{Mg_{1-x}Zr_xH_2} - N_{Mg_{1-x}Zr_x}E_{Mg_{1-x}Zr_x} - N_{H_2}E_{H_2}\right) / N_{Mg_{1-x}Zr_x} \quad (2)$$

Where $E_{Mg_{1-x}Zr_xH_2}$, $E_{Mg_{1-x}Zr_x}$, E_{H_2}, is the energy of the $Mg_{1-x}Zr_xH_2$, $Mg_{1-x}Zr_x$, H_2, respectively. $N_{Mg_{1-x}Zr_x}$, N_{H_2} corresponds to the number of the $Mg_{1-x}Zr_x$ and H_2, respectively. The formation energy (see Table 2) is even lower as the number of Zr layers increases, implying that the Zr-containing system is more prone to hydrogen absorption.

For these calculations, density functional theory (DFT) within the generalized gradient approximation (GGA) as implemented in the Vienna *ab initio* simulations package (VASP) [33,34] was used. Perdew-Burke-Ernzerhof (PBE) [35] potentials and a cutoff energy of 520 eV for the plane-wave basis set were employed. $4 \times 4 \times 1$ Monkhorst-Pack *k*-point grid [36] was used for the calculation of the slabs. The criterion of energy and force is minimized to 1×10^{-5} eV and 0.001 eV/Å, respectively. VASPKIT [37] and VESTA [38] were also employed for analysis.

Table 1
The corresponding parameters of MgH_2, ZrH_2 unit cell.

	Space group	2θ of (0002)/(111) in XRD	Parameters of primitive cell (Å)	*d* (Å)
MgH_2	$Fm\bar{3}m$, No. 225	32.567°	$a = b = c = 3.367$	2.749
ZrH_2	$Fm\bar{3}m$, No. 225	32.176°	$a = b = c = 3.407$	2.782

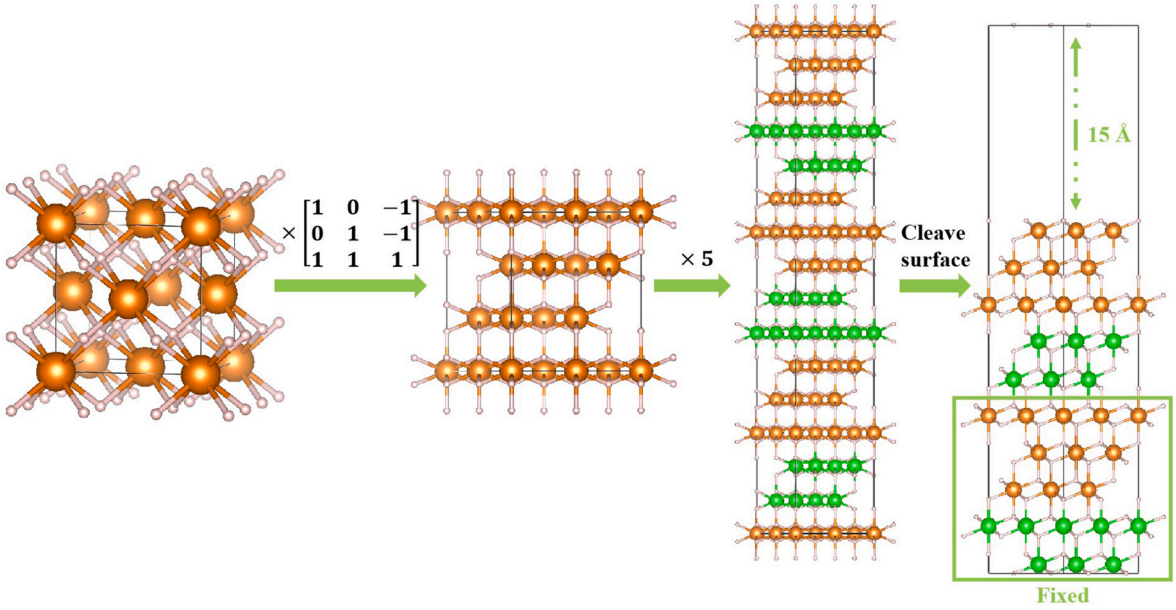

Fig. 1. The procedure to construct $Mg_{0.83}$-$Zr_{0.17}H_2$(111) slab. Color legend: Mg, orange; Zr, green; H, pink. (For interpretation of the references to color in this figure legend, the reader is referred to the Web version of this article.)

Table 2
The structural parameters and formation energies of the $Mg_{1-x}Zr_xH_2$ (x = 0, 0.17).

System	N_{Mg}	N_{Zr}	N_H	a[Å]	b[Å]	c[Å]	angles (degrees)	E_{form} (eV/f.u.)
pure-MgH_2	60	0	120	6.72	6.72	41.17	α = β = 90.00,γ = 60	−0.199
$Mg_{0.83}$-$Zr_{0.17}H_2$	36	24	120	6.65	6.65	42.61	α = β = 90.00,γ = 60	−0.900

3. Results and discussion

3.1. Structures of surfaces

The geometric and electronic structures of pure-MgH_2(111) and $Mg_{0.83}$-$Zr_{0.17}H_2$(111) surfaces are discussed in this section. The bottom 5 layers of the two slabs are both fixed to simulate the bulk phase while the upper five layers of atoms are relaxed, as shown in Fig. 2. It is clear that the overall interlayer spacing of $Mg_{0.83}$-$Zr_{0.17}H_2$(111) surfaces has expanded, and the atomic interlayer spacing also varies greatly. The distance between two Zr atomic layers is the largest, up to 2.94 Å (d_{45}), while the distance between Mg atomic layer and adjacent Zr atomic layer is the smallest, as low as 2.78 Å (d_{34}). For pure-MgH_2(111) slab, The average interlayer spacing of system a is around 2.74 Å, which is 0.10 Å lower than that of $Mg_{0.83}$-$Zr_{0.17}H_2$(111). Relative to the fixed atomic slabs, the relaxed layers in the pure-MgH_2(111) slab exhibit a

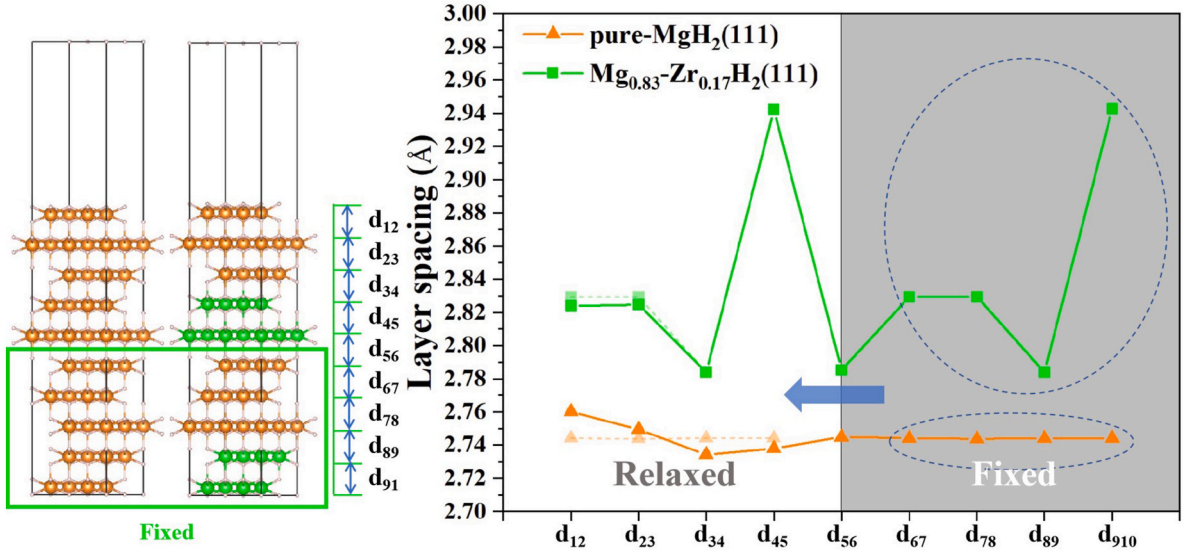

Fig. 2. Layer arrangement of (a) Mg_{1-x}-Zr_xH_2(111) slabs, with (b) the corresponding layer spacing. Here d_{12} stands for the spacing between the 1st and 2nd layer, and corresponding for other d_{mn} (m = 1–9, $n = m + 1$). Color legend: Mg, orange; Zr, green; H, pink. (For interpretation of the references to color in this figure legend, the reader is referred to the Web version of this article.)

more pronounced variation in spacing than those in $Mg_{0.83}$-$Zr_{0.17}H_2$(111). Evidently, the outermost surface of pure-MgH_2(111) slab expands by 0.55 % into the vacuum region. These enlarged inter-layer spacings are likely to stretch the Mg–H bond lengths, thereby weakening the metal-hydrogen interaction and facilitating dehydrogenation.

While the evolution of layer spacings offers an indirect hint that Mg–H bond lengths are being elongated, the two-dimensional (2D) charge density plots provide a more direct, electronic-scale view of how Zr incorporation modifies the bonding environment. Deformation charge density difference (see Fig. 3) demonstrates that the charges of H atom which bonded with Zr is no longer localized, the positive charge is distributed around H atoms, as shown in Fig. 3b. This is very different from the pure-MgH_2(111) system (see Fig. 3a). The presence of Zr atomic layer in the modulation structure leads to changes in the local electronic structure, and the difference in electronegativity between it and the matrix atoms Mg causes electrons to migrate and redistribute, resulting in a complex and blurred distribution of charge density around the atoms.

Comparison of the partial denstiy of states (PDOS) in Fig. 4 reveals that the H *s* orbitals become more and more localized and sharp as the presence of Zr. Between −7.00 and −4.00 eV, five distinct hybridisation peaks are resolved in $Mg_{0.83}$-$Zr_{0.17}H_2$(111) system, each corresponding to overlapping Zr *d* and H *s* states that characterise the covalent component of the Zr–H bond. The energy range occupied by the total density of states of the pure-MgH_2(111) system is from −10.11 to 5.87 eV, and finally the range of the $Mg_{0.83}$-$Zr_{0.17}H_2$(111) system narrows to −10.07–4.22 eV. Compared with the pure-MgH_2(111) system, there are more electronic states contributed by the Zr *d* orbital from the $Mg_{0.83}$-$Zr_{0.17}H_2$(111) system near the Fermi level, indicating the latter exhibits metallicity.

3.2. Hydrogen desorption properties

The above calculations indicate that the dehydrogenation of atomic H in the first layer, Mg–Mg interface, Mg–Zr interface, Zr–Zr interface are rather different during the whole dehydrogenation. Inspired by this, we employed the COHP method [39,40] to analyze the electronics and energetics of various Mg–H bonds. The integrated crystal orbital Hamilton population (ICOHP) of the Mg–H bonds involved in the H_2 desorption process were calculated. The -ICOHPs of each bond were calculated to analyze the change of Mg–H bond strength more clearly.

As shown in Fig. 5, the strengths of the Mg–H bonds are various in various layers of various systems. It is clear that the bonds 1-II, exploring to vacuum, are strong with an -ICOHP value of about 0.63, larger than most of the Mg–H bonds inside for both two systems. This observation is in accordance with the results obtained by Dong et al., who identified

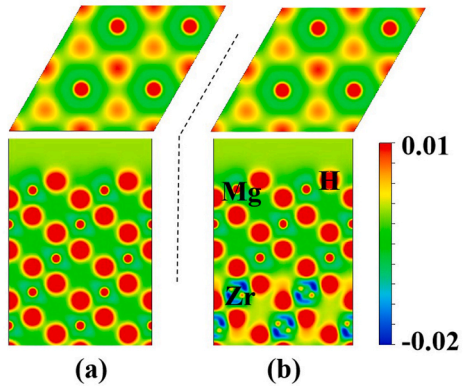

Fig. 3. Deformation charge density difference for (a) pure-MgH_2(111), (b) $Mg_{0.83}$-$Zr_{0.17}H_2$(111) slabs. The unit for the color bar is e/Bohr [3]. (For interpretation of the references to color in this figure legend, the reader is referred to the Web version of this article.)

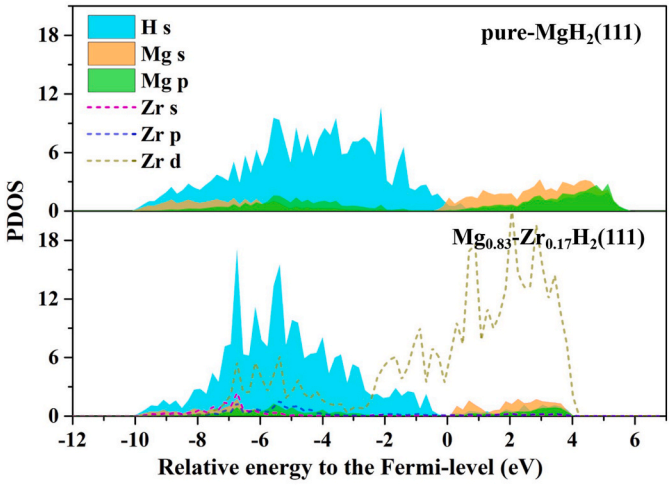

Fig. 4. PDOS of various elements in pure-MgH_2(111) and $Mg_{0.83}$-$Zr_{0.17}H_2$(111) systems.

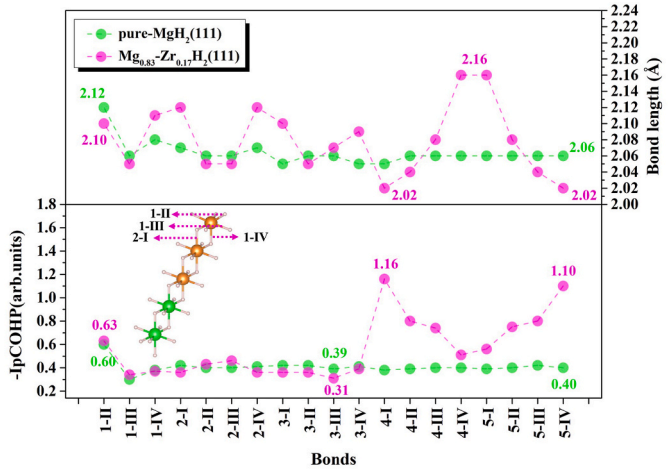

Fig. 5. Bond length (top figure) and ICOHP (bottom figure) of Mg–H, Zr–H bonds in pure-MgH_2(111) and $Mg_{0.83}$-$Zr_{0.17}H_2$(111) systems. The inset graphs show the difference in the bond length and strength of all Mg–H (Zr–H) bonds in various layers. 1 to 5 means which layer of metal atoms this is, and I to IV correspond to various Mg(Zr)–H bonds.

that the dehydrogenation process occurring on the surface of magnesium hydride exhibits the most significant energy barrier [41]. Besides, the strengths of Zr–H bonds in the Mg–Zr interface, such as bonds 4-I and 5-IV of the $Mg_{0.83}$-$Zr_{0.17}H_2$(111) slabs are very strong, consistent with the report [42] by Pozzo et al. The corresponding ICOHP values are all above 1.00. Especially for the Zr–H bond 4-I in the $Mg_{0.83}$-$Zr_{0.17}H_2$(111) slabs, it has a bond length as low as 2.02 Å and a bond strength as high as 1.16. This may be the reason why Mg–Zr–H system cannot be completely dehydrogenated at 250 °C[31]. As the Zr–H bonds are too strong to break at this temperature and requires a higher one. It corresponding to the report [29] of Ding et al. that the Zr–H bonds is hard to break. Moreover, there show a significant weakening of the bond strength of the 3-III (Mg–H bond in the Mg–Zr co-lattice layer) in the $Mg_{0.83}$-$Zr_{0.17}H_2$(111) slab. Xiao et al. found that Zr forms stronger covalent bonds with hydrogen (H) due to its higher electronegativity and ability to accept electrons [43]. Thus this stronger interaction between Zr and H weakens the existing bonds between Mg and H. This is consistent with the experiment [31], where the Mg–H bonds at the Mg–Zr co-lattice interface break first. Regrettably, it has been observed that while the more readily breakable Mg–H bonds at the Mg–Zr

coherent interfaces significantly lower the initial dehydrogenation temperature of the thin film, the introduction of the more robust Zr–H bonds dictates a higher temperature requirement for complete dehydrogenation. In terms of the quantitative ratio of bond numbers, the Zr–H bonds (8 out of 19) are twice as numerous as the weakened Mg–H bonds (4 out of 19).

4. Conclusions

This study investigates the hydrogen desorption properties of $Mg_{0.83}$-$Zr_{0.17}H_2$(111) semi-co-sputtering films using first-principles calculations. We analyzed the interlayer spacing, bond lengths, and bond strengths of pure-MgH_2(111) and $Mg_{0.83}$-$Zr_{0.17}H_2$(111) slabs. The calculation results align with the experimental conclusion that the Mg–Zr co-lattice interface is preferentially dehydrogenated as the presence of Zr weakens the surrounding Mg–H bonds. Electronic structure analysis further support this conclusion: Zr additions creates an anisotropic charge density distribution around hydrogen atoms, causing boundaries to become blurred and irregular. Additionally, H *s* orbitals become increasingly localized and sharp at the same time. Corresponding ICOHP values confirm the relatively weaker Mg–H bond strengths at the coherent interface between Mg and Zr layers.

CRediT authorship contribution statement

Yongqing Wang: Writing – original draft. **Junqing Ding:** Data curation. **Zhijie Fang:** Software. **Xingyu Zhou:** Writing – review & editing. **Yu-Jun Zhao:** Supervision.

Declaration of competing interest

The authors declare that they have no known competing financial interests or personal relationships that could have appeared to influence the work reported in this paper.

Acknowledgements

This work is financially supported by the Guangxi Natural Science Foundation (Grant No. 2024GXNSFBA010243), the National Natural Science Foundation of China (Grant No. 12364011), the Guangxi Science and Technology Plan (Grant No. AD25069027), the Liuzhou Science and Technology Program (Grants No. 2023PRJ0103, 2024AA0204A001), the Opening Project of Guangxi Key Laboratory of Multidimensional Information Fusion for Intelligent Vehicles (Grant No. 2025OP07) and the Doctoral Foundation Project of Guangxi University of Science and Technology (Grants No. 20Z41, 25Z12).

References

[1] Schlapbach Louis, et al. Hydrogen-storage materials for Mobile applications. Nature 2001;414:353–8. https://doi.org/10.1038/35104634.
[2] Schuth F, et al. Light metal hydrides and complex hydrides for hydrogen storage. Chem Commun 2004:2249–58. https://doi.org/10.1039/b406522k.
[3] Sakintuna Billur, et al. Metal hydride materials for solid hydrogen storage: a review. Int J Hydrogen Energy 2007;32:1121–40. https://doi.org/10.1016/j.ijhydene.2006.11.022.
[4] Chen Ping, et al. Recent progress in hydrogen storage. Mater Today 2008;11:36–43. https://doi.org/10.1016/s1369-7021(08)70251-7.
[5] Eberle Ulrich, et al. Chemical and physical solutions for hydrogen storage. Angew Chem, Int Ed 2009;48:6608–30. https://doi.org/10.1002/anie.200806293.
[6] Yu Xuebin, et al. Recent advances and remaining challenges of nanostructured materials for hydrogen storage applications. Prog Mater Sci 2017;88:1–48. https://doi.org/10.1016/j.pmatsci.2017.03.001.
[7] Abe JO, et al. Hydrogen energy, economy and storage: review and recommendation. Int J Hydrogen Energy 2019;44:15072–86. https://doi.org/10.1016/j.ijhydene.2019.04.068.
[8] Jain IP, et al. Novel hydrogen storage materials: a review of lightweight complex hydrides. J Alloys Compd 2010;503:303–39. https://doi.org/10.1016/j.jallcom.2010.04.250.
[9] Rusman NAA, et al. A review on the current progress of metal hydrides material for solid-state hydrogen storage applications. Int J Hydrogen Energy 2016;41:12108–26. https://doi.org/10.1016/j.ijhydene.2016.05.244.
[10] Jain IP, et al. Hydrogen storage in Mg: a most promising material. Int J Hydrogen Energy 2010;35:5133–44. https://doi.org/10.1016/j.ijhydene.2009.08.088.
[11] Yartys VA, et al. Magnesium based materials for hydrogen based energy storage: past, present and future. Int J Hydrogen Energy 2019;44:7809–59. https://doi.org/10.1016/j.ijhydene.2018.12.212.
[12] Zaluska A, et al. Nanocrystalline magnesium for hydrogen storage. J Alloys Compd 1999;288:217–25. https://doi.org/10.1016/s0925-8388(99)00073-0.
[13] Liang G. Synthesis and hydrogen storage properties of Mg-based alloys. J Alloys Compd 2004;370:123–8. https://doi.org/10.1016/j.jallcom.2003.09.031.
[14] Czujko T, et al. Investigation of the hydrogen desorption properties of Mg+10 wt.% X (X = V, Y, Zr) submicrocrystalline composites. J Alloys Compd 2006;414:240–7. https://doi.org/10.1016/j.jallcom.2005.07.009.
[15] Checchetto R, et al. Catalytic properties on the hydrogen desorption process of metallic additives dispersed in the MgH_2 matrix. J Alloys Compd 2007;446–447:58–62. https://doi.org/10.1016/j.jallcom.2006.11.017.
[16] Malka IE, et al. A study of the ZrF_4, NbF_5, TaF_5, and $TiCl_3$ influences on the MgH_2 sorption properties. Int J Hydrogen Energy 2011;36:12909–17. https://doi.org/10.1016/j.ijhydene.2011.07.020.
[17] Wang Yongqing, et al. Study on catalytic effect and mechanism of MOF (MOF = ZIF-8, ZIF-67, MOF-74) on hydrogen storage properties of magnesium. Int J Hydrogen Energy 2019;44:28863–73. https://doi.org/10.1016/j.ijhydene.2019.09.110.
[18] Qu Jianglan, et al. Superior hydrogen absorption and desorption behavior of Mg thin films. J Power Sources 2009;186:515–20. https://doi.org/10.1016/j.jpowsour.2008.10.079.
[19] Qu Jianglan, et al. Improved hydrogen storage properties in Mg-based thin films by tailoring structures. Int J Hydrogen Energy 2010;35:8331–6. https://doi.org/10.1016/j.ijhydene.2009.12.007.
[20] Gharavi Ayshe G, et al. Thickness effects in hydrogen sorption of Mg/Pd thin films. J Alloys Compd 2013;580:S175–8. https://doi.org/10.1016/j.jallcom.2013.02.120.
[21] Higuchi K, et al. In situ study of hydriding-dehydriding properties in some Pd/Mg thin films with different degree of Mg crystallization. J Alloys Compd 1999;293:484–9. https://doi.org/10.1016/S0925-8388(99)00470-3.
[22] Qu J, et al. A kinetics study on promising hydrogen storage properties of Mg-based thin films at room temperature. Dalton Trans 2014;43:5908–12. https://doi.org/10.1039/c3dt53646g.
[23] Xin G, et al. Superior (de)hydrogenation properties of mg-ti-pd trilayer films at room temperature. Dalton Trans 2012;41:6783–90. https://doi.org/10.1039/c2dt30253e.
[24] Akyıldız Hasan, et al. Hydrogen sorption in crystalline and amorphous Mg–Cu thin films. J Alloys Compd 2010;492:745–50. https://doi.org/10.1016/j.jallcom.2009.12.037.
[25] Ouyang LZ, et al. Microstructure of MmM_5/Mg multi-layer films prepared by magnetron sputtering. J Alloys Compd 2005;404–406:485–9. https://doi.org/10.1016/j.jallcom.2005.01.120.
[26] Kyoi Daisuke, et al. Synthesis of FCC Mg–Zr and Mg–Hf hydrides using GPa hydrogen pressure method and their hydrogen-desorption properties. J Alloys Compd 2008;463:311–6. https://doi.org/10.1016/j.jallcom.2007.09.004.
[27] Bazzanella Nicola, et al. Catalytic effect of mixed Zr–Fe additives on the hydrogen desorption kinetics of MgH_2. Appl Phys Lett 2008;92:051910. https://doi.org/10.1063/1.2840180.
[28] Okamoto H. Mg-Zr (Magnesium-Zirconium). J Phase Equilibria Diffus 2007;28:305–6. https://doi.org/10.1007/s11669-007-9060-7.
[29] Ding Xiaoli, et al. Hydrogen-induced magnesium–zirconium interfacial coupling: enabling fast hydrogen sorption at lower temperatures. J Mater Chem A 2017;5:5067–76. https://doi.org/10.1039/c7ta00460e.
[30] Bao Shanhu, et al. Switchable mirror based on mg–zr–h thin films. J Alloys Compd 2012;513:495–8. https://doi.org/10.1016/j.jallcom.2011.10.098.
[31] Qin Jiayao, et al. Construction of Mg/Zr superlattice structure to achieve efficient hydrogen storage via atomic-scale interaction in Mg-Zr modulation films. Acta Mater 2024;263:119470. https://doi.org/10.1016/j.actamat.2023.119470.
[32] Jain Anubhav, et al. Commentary: the materials project: a materials genome approach to accelerating materials innovation. APL Mater 2013;1. https://doi.org/10.1063/1.4812323.
[33] Kresse G, et al. Efficient iterative schemes for ab initio total-energy calculations using a plane-wave basis set. Phys Rev B 1996;54:11169–86. https://doi.org/10.1103/PhysRevB.54.11169.
[34] Kresse G, et al. Efficiency of ab-initio total energy calculations for metals and semiconductors using a plane-wave basis set. Comput Mater Sci 1996;6:15–50. https://doi.org/10.1016/0927-0256(96)00008-0.
[35] Perdew John P, et al. Generalized gradient approximation made simple. Phys Rev Lett 1996;77:3865–8. https://doi.org/10.1103/PhysRevLett.77.3865.
[36] Monkhorst Hendrik J, et al. Special points for Brillouin-zone integrations. Phys Rev B 1976;13:5188–92. https://doi.org/10.1103/PhysRevB.13.5188.
[37] Wang Vei, et al. VASPKIT: a user-friendly interface facilitating high-throughput computing and analysis using VASP code. Comput Phys Commun 2021;267:108033. https://doi.org/10.1016/j.cpc.2021.108033.
[38] Momma Koichi, et al. VESTA 3 for three-dimensional visualization of crystal, volumetric and morphology data. J Appl Crystallogr 2011;44:1272–6. https://doi.org/10.1107/s0021889811038970.

[39] Deringer Volker L, et al. Crystal orbital hamilton population (COHP) analysis as projected from plane-wave basis sets. J Phys Chem A 2011;115:5461–6. https://doi.org/10.1021/jp202489s.
[40] Dronskowski Richard, et al. Crystal orbital hamilton populations (COHP): energy-resolved visualization of chemical bonding in solids based on density-functional calculations. J Phys Chem 1993;97:8617–24. https://doi.org/10.1021/j100135a014.
[41] Dong Shuai, et al. The “burst effect” of hydrogen desorption in MgH2 dehydrogenation. J Mater Chem A 2022;10:22363–72. https://doi.org/10.1039/d2ta06458h.
[42] Pozzo M, et al. Hydrogen dissociation and diffusion on transition metal (=Ti, Zr, V, Fe, Ru, Co, Rh, Ni, Pd, Cu, ag)-doped Mg(0001) surfaces. Int J Hydrogen Energy 2009;34:1922–30. https://doi.org/10.1016/j.ijhydene.2008.11.109.
[43] Xiao Xiao-Bing, et al. Energetics and electronic properties of Mg_7TMH_{16} (TM=Sc, Ti, V, Y, Zr, Nb): an ab initio study. Phys B Condens Matter 2009;404:2234–40. https://doi.org/10.1016/j.physb.2009.04.013.